41st Aerospace Sciences Meeting and Exhibit
6-9 January 2003, Reno, Nevada

AIAA 2003-780

LES of Turbulent Jets using the Lattice Boltzmann Approach

H. Feiz*, J. H. Soo† and S. Menon‡
School of Aerospace Engineering
Georgia Inst. of Technology
Atlanta, Georgia, USA 30332

Three dimensional large-eddy simulations (LES) of a forced square jet and a square jet-in-cross-flow (JICF) are conducted using the 19-bit Lattice Boltzmann Equation (LBE) method. A localized, dynamic algebraic subgrid model is used to extend the LBE method to LES. In all simulations, the upstream jet inlet is also resolved. Thus, interactions at the jet exit plane occur naturally. Simulation of the forced jet shows that the shed coherent structures undergo multiple axis switching in the jet increasing the effective mixing. The overall features are in agreement with past experiments for a similar configuration. JICF results are also compared with data and with other numerical method results. Good agreement with data is again obtained in the present study. These results establish LBE-LES as an alternate method for simulating turbulent shear flows. The strengths and limitations of the LBE-LES are also discussed.

1 Introduction

Improvements in gas turbine engine design are needed to meet the increasingly stringent federal and international emission laws. Fuel efficient, low-NOx gas turbine systems are being investigated to meet these laws. Lean combustion systems have the potential for meeting these goals. However, one consequence of lean burning is that as the equivalence ratio of the fuel-air mixture is reduced, small turbulent fluctuations in the flow can have a major effect on the flame leading to the phenomenon called Lean-Blow Out (LBO). During LBO, the flame first undergoes local and then, global extinction. Sometimes (and depending on many known and unknown parameters), LBO is accompanied by an increase in pressure fluctuations leading to combustion instability. LBO has been observed in gaseous premixed systems as well as in liquid fuelled gas turbines. Therefore, this is a fundamental feature in gas turbine engines. Understanding and controlling LBO (or perhaps increasing the lean stable flammability limit) would lead to more efficient combustion systems. Recent studies employing active control[1,2,3] are focussed on controlling fuel-air mixing and/or flame propagation so that stable lean burning systems can be achieved.

Active control using fuel modulation has been shown to be an effective approach both experimentally[1] and numerically.[4] Numerical simulations can help in the design cycle if the physics of LBO and active control can be accurately computed. Computational efficiency is very important since there are many parameters (design, placement and forcing conditions) that have to be optimized and there is a wide range of physical dimensions that must be resolved. For example, a typical fuel injector orifice can be as small as 1-5 mm and therefore, the micro-scale actuators have to be much smaller than this scale (and hence, these devices are MEMS-scale devices). The flow both inside and outside the actuator must be resolved in order to capture the dynamics of the momentum injection process. On the other hand, to study fuel air mixing (and perhaps combustion), flow in the combustor (with a length of around 30 cm) also have to be simulated. The resolution requirement to resolve the synthetic jet embedded inside the fuel injector and the flow outside in the combustor is too severe for any single numerical method.

The Lattice Boltzmann Equation (LBE) method has the potential to provide a collaborative resolution to this multi-scale problem.[5,6] LBE has been used successfully to simulate many fluid dynamic problems[7,8] and is seen as an attractive alternative to conventional finite-difference scheme because it recovers the Navier-Stokes equations, and is computationally very efficient, more stable, and easily parallelizable. In recent studies,[4] a two-dimensional LBE method was developed and demonstrated for DNS of synthetic jet flows. Studies with synthetic jets embedded within the fuel injector were also carried out and it was shown that fuel-air mixing can be considerably enhanced by synthetic jet actuation.

This paper reports on the development of a full 3D LBE model for direct (DNS) and large-eddy simulations (LES). The eventual goal is to combine the LBE-LES with a conventional finite-volume LES (FV-

*Student Member, AIAA
†Graduate Research Assistant
‡Professor, Associate Fellow, AIAA

LES) whereby, the LBE-LES model is used in regions where very fine-scale features have to be resolved (e.g., inside the embedded synthetic jets and the fuel injector) and FV-LES is used in the combustor. The FV-LES approach is a well established method already operational[9] and the present study will demonstrate the ability of the LBE-LES.

In this paper, LBE-LES of square jets and square jets in cross flow are conducted and compared to available data. Square jets are simulated here since it is well known that mixing enhancement increases when non-circular jets are employed.[10,11] This enhancement is shown to be in part, due to the axis-switching mechanism triggered by non-uniform self-induction of the large-scale structures shed from the jet exit. Experimentally and numerically, this feature has been observed in elliptic jet,[12] rectangular jet,[13] square jet.[14,15] Jet in cross flow is also a canonical flow that models fuel jet injection in realistic devices. In addition, jet in cross flow (JICF) occurs in other real applications, such as, V/STOL aircraft, internal cooling of turbine blades, dilution air jets in combustion chamber of gas turbine engines, etc. The square jet in cross-flow simulated here is a test configuration that was studied both experimentally[16] and numerically[17] in the past, and therefore, data exists for validation.

2 LBE Formulation

The LBE method originates from a Boolean fluid model known as the lattice gas automata (LGA) which simulates viscous fluid flow by tracing the fluid motion through advection of fluid particles and particle collision on a regular lattice. LBE is an improvement over LGA in which the Boolean fluid model is replaced by a single continuous particle distribution, which is analogous to the particle distribution function in kinetic theory. This replacement eliminates the intrinsic noise inherent in LGA schemes and overcomes the shortcomings of a limited transport coefficient. The introduction of the BGK single relaxation time model for the collision operator further simplifies the algorithm and eliminates the lack of Galilean invariance and the dependence of pressure on velocity.[7,18] This model assumes that the particle distribution function relaxes to its equilibrium state at a constant rate, and the collision operator is similar to the classical BGK Boltzmann operator.[19]

Since its introduction, the LBE method has been shown to be a competitive method in solving computational fluid dynamics (CFD) problems. Whereas conventional Navier-Stokes schemes solve the macroscopic properties of the fluid explicitly, LBE method solves the Boltzmann equation by tracking the evolution of the microscopic particle distribution of the fluid in phase space (velocity space, physical space and time). Consequently, the conserved variables of the fluid (density and momentum) are obtained indirectly by local integration of the particle distribution (over the velocity space). The incompressible Navier-Stokes is recovered in the nearly incompressible limit of LBE using the Chapman-Enskog expansion.

Solving the lattice Boltzmann equation instead of the Navier-Stokes equation provides three distinct advantages. First, due to the kinetic nature of the LBE method, the convection operator is linear. Simple convection in conjunction with a collision process allows the recovery of the nonlinear macroscopic advection through multi-scale expansions. Second, because the macroscopic properties of the flow field is not solved directly, LBE method avoids solving the Poisson equation, which proves to be numerically difficult in most finite difference methods. Third, the macroscopic properties are obtained from the microscopic particle distributions through simple arithmetic integration. Interested readers seeking further information on LBE are referred to a recent review.[8]

2.1 The Governing Equations

LBE method consists of two primary steps. The particles first stream to its next nearest neighbor in the direction of its prescribed velocity. Subsequently, particles of different velocities arriving at the same node interacts with each other by relaxing to its local equilibrium values which are formulated specifically to recover the low Mach number limit of the Navier-Stokes equation. The evolution of the non-dimensional distribution function f_α is thus governed by:

$$f_\alpha(\mathbf{x}+\mathbf{e}_\alpha\delta, t+\delta) - f_\alpha(\mathbf{x},t) = \frac{1}{\tau}[f_\alpha^{eq}(\mathbf{x},t) - f_\alpha(\mathbf{x},t)],$$

$$\alpha = 0, 1, \cdots, 18 \qquad (1)$$

where τ is the relaxation time, f_α^{eq} is the equilibrium distribution function and e_α is the particle speed in α direction. The characteristic speed is thus $c = \mathbf{e}_\alpha\delta/\delta = |\mathbf{e}_\alpha|$. Rest particles of type 0 with $e_0 = 0$ are also allowed. Note that the time step and the lattice spacing each have equal spacing of unity. Thus, $\delta = 1$.

In principle, there are an infinite number of possible velocity directions in the 3D velocity space. Discretizing these infinite number of velocity directions into a fixed set of velocity directions inevitably introduces discretization errors to the solution. As a general rule, the accuracy of the model to simulate Navier-Stokes flow comes at the expense of increasing computational cost resulting from the number of discrete velocities used in the model. Frisch et al.[20] have shown that the Navier-Stokes equation cannot be recovered unless sufficient discrete velocities is used to ensure lattice symmetry.

There are various 3D cubic lattice models developed, most notably the 15-bit (D315), 19-bit(D3Q19), and 27-bit(D3Q27) model.[21] Here, using common notations in scientific literatures, D is the number of

dimensions and Q is the number of discrete velocities. A variant model can be derived from each model by removing the rest particle, resulting in models D3Q14, D3Q18, and D3Q26. There models are used less frequently because LBE models with a rest velocity generally have better computational stability. In previous numerical simulations of a square duct, a lid-driven cavity and a circular pipe,[22] no significant improvement in accuracy is observed when the D3Q27 model was used over the D3Q19 model, and thus, the D3Q19 model is assumed to be sufficiently accurate for the current purpose.

The 19-bit velocity field (Fig. 1) is:

$$\mathbf{e}_\alpha = \begin{cases} (0,0,0) \\ \text{for } \alpha = 0, \text{ rest particle,} \\ ((\pm 1,0,0),(0,\pm 1,0),(0,0,\pm 1))c \\ \text{for } \alpha = 1,2,\cdots,6, \text{ class I links,} \\ ((\pm 1,\pm 1,0),(0,\pm 1,\pm 1),(\pm 1,0,\pm 1))\sqrt{2}c \\ \text{for } \alpha = 7,8,\cdots,18, \text{ class II links.} \end{cases} \tag{2}$$

Here, f_α^{eq} is given by the following form:

$$f_\alpha^{eq} = w_\alpha \rho [1 + \frac{3(\mathbf{e}_\alpha \cdot \mathbf{u})}{c^2} + \frac{9}{2}\frac{(\mathbf{e}_\alpha \cdot \mathbf{u})^2}{c^4} - \frac{3}{2}\frac{\mathbf{u}^2}{c^2}], \tag{3}$$

where

$$w_\alpha = \begin{cases} \frac{1}{3} & \alpha = 0 \\ \frac{1}{18} & \alpha = 1,2,\cdots,6 \\ \frac{1}{36} & \alpha = 7,8,\cdots,18. \end{cases}$$

The macroscopic properties of the flow field can be obtained by integrating the distribution functions over the velocity space:

$$\rho = \sum_\alpha f_\alpha \tag{4}$$

$$\rho \mathbf{u} = \sum_\alpha \mathbf{e}_\alpha f_\alpha, \qquad \alpha = 0,1,...,18 \tag{5}$$

where ρ is the density and $\mathbf{u}$ is the velocity. All macroscopic properties are obtained as function of space and time from this integration.

The Navier-Stokes mass and momentum equations are obtained by using the BGK single relaxation time model,[19] and by employing Chapman-Enskog on Eq. (2.1) are:

$$\frac{\partial \rho}{\partial t} + \frac{\partial \rho u_i}{\partial x_i} = 0 \tag{6}$$

$$\frac{\partial(\rho\ u_i)}{\partial t} + \frac{\partial \rho u_i u_j}{\partial x_j} = \frac{\partial(c_s^2 \rho)}{\partial x_i} + \frac{\partial 2\nu\rho S_{ij}}{\partial x_j} \tag{7}$$

Here, repeated indices indicate summation and $S_{ij} = \frac{1}{2}(\partial \tilde{u}_i/\partial x_j + \partial \tilde{u}_j/\partial x_i)$ is the strain-rate tensor. The non-dimensional pressure is given by the constant temperature ideal gas equation of state $p = c_s^2 \rho$ where c_s is the speed of sound with $(c_s = c/\sqrt{3})$, and $\nu = [(2\tau - 1)/6]$ is the kinematic viscosity.

2.2 Subgrid Model

In this study, a LES version of the LBE model is developed for application to high-Re flows. Spatial filtering reduces the high wave number Fourier components of the particle distribution and separates the resolved scale parts from the unresolved scales. For high Reynolds flow, LES is accomplished by solving the "filtered" form of the LBE equation (LBELES):

$$\bar{f}_\alpha(\mathbf{x} + \mathbf{e}_\alpha \delta, t + \delta) - \bar{f}_\alpha(\mathbf{x}, t) = \frac{1}{\tau_{sgs}}[\bar{f}_\alpha^{eq}(\mathbf{x}, t) - \bar{f}_\alpha(\mathbf{x}, t)]$$

$$\alpha = 0,1,\cdots,18 \tag{8}$$

where the distribution function $\bar{f}_\alpha$ represents only those of the resolved scales. The effect of the unresolved scale motion is modelled through an effective collision term. The form of the subgrid correction is not fully explored at present. In conventional LES models based on the one-equation model for the subgrid kinetic energy[9] have proven quite robust. However, a more simpler model based on an algebraic representation of the eddy viscosity model (based on the Smagorinsky's eddy viscosity model) is adopted for the present effort. Using this model, the effective viscosity is obtained as follows:

$$\nu + \nu_\tau = \frac{2\tau_{sgs} - 1}{6} \tag{9}$$

with the eddy viscosity ν_τ determined using:

$$\nu_\tau = C_\nu \overline{\Delta}^2 S \tag{10}$$

where C_ν is the Smagorinsky constant, $\overline{\Delta} = (\Delta_x \Delta_y \Delta_z)^{\frac{1}{3}}$ is the associated length scale and $S = |\bar{S}_{ij}\bar{S}_{ij}|$. Here, $\bar{S}_{ij} = \frac{1}{2}(\partial \bar{u}_i/\partial x_j + \partial \bar{u}_j/\partial x_i)$ is the resolved-scale rate-of-strain tensor is the characteristic filtered rate of strain tensor.

The Smagorinsky constant C_ν is determined using the localized dynamic model (LDM),[9,23] which was developed for the k-equation model but now adapted to the Smagorinsky model. The LDM is formulated based on the assumption of scale similarity in the inertial subrange. Provided that enough of the inertial subrange is resolved, stresses at the cutoff (i.e., the grid size) can be related to stresses at say, twice the cutoff (i.e., the test filter width). This then defines a scale level where explicit filtering is required. The test-scale field is constructed from the grid-scale field by applying a test filter which is characterized by $\widehat{\Delta}$ (typically, $\widehat{\Delta} = 2\bar{\Delta}$ with $\bar{\Delta}$ the characteristic grid size). In the following, the application of the test filter on a variable ϕ is denoted by $\widehat{\phi}$ and the test-scale Favre-filtered variable is denoted by $\langle\phi\rangle = \widehat{\bar{\rho}\phi}/\widehat{\bar{\rho}}$.

C_ν is obtained using

$$C_\nu = \frac{L'_{ij} M_{ij}}{2 M_{ij} M_{ij}} \tag{11}$$

where $L'_{ij} = L_{ij} - \frac{2}{3}\widehat{\rho}k^{test}\delta_{ij}$ and $M_{ij} = -\widehat{\rho}\sqrt{k^{test}}\widehat{\Delta}(\langle\tilde{S_{ij}}\rangle - \frac{1}{3}\langle\tilde{S_{kk}}\rangle\delta_{ij})$. Here, $L_{ij} = \widehat{\rho}(\langle\tilde{u}_i\tilde{u}_j\rangle - \langle\tilde{u}_i\rangle\langle\tilde{u}_j\rangle)$ is the Leonard stress tensor and $k^{test} = \frac{1}{2}(\langle\tilde{u}_i\tilde{u}_j\rangle - \langle\tilde{u}_i\rangle\langle\tilde{u}_j\rangle) = \frac{1}{2}L_{kk}/\widehat{\rho}$ is the resolved kinetic energy at the test-filter level.

As noted later, the algebraic model has some inherent limitations in conventional LES and these limitations remain in effect in the LBE-LES approach. Thus, for high Re flows, the lattice resolution has to be considerable since the algebraic model requires that nearly all of the inertial range is resolved. The alternate one-equation model[23] has the ability to deal with high-Re flows on relatively coarse grid and therefore, we will be implementing this option in the near future.

2.3 Boundary Conditions

The accuracy of the LBE and LBE-LES models depend strongly on the proper implementation of the boundary conditions. This is particularly true for complex geometries. In general, the most problematic boundary condition is the no-slip condition. The most commonly used method to apply a no-slip boundary condition is the particle bounce-back scheme, that is, the particles arriving at the stationary wall is reflected back in the direction it came from. Although easy to implement, the exact location of the no-slip wall is in question. The bounce-back scheme exhibited second-order accuracy only when the no-slip wall is placed at exactly halfway between the boundary node and the first fluid node in numerical simulations of Poiseuille flow using the D2Q9 and D3Q15 models.[24] Since more discrete velocity links (19) are used in the 3D model, the boundaries are required to be as accurate in the present study. In any case, the error associated with the wall location cannot be larger than the grid size, and by grid clustering near the wall boundaries, this error is minimized.

These boundary conditions were originally developed for the D2Q6 model,[25] and were later adapted to the present D3Q19 model.[26] Adaptation is necessary because additional rules are needed to solve for the unknown incoming populations for models with more numerous links then the D2Q6 model. In particular, at the end of the streaming step and prior to the collision, populations of the outward pointing links and those which run parallel to the boundary surface are known whereas the inward pointing ones are unknown. Thus, bounce-back prescribes provisional populations for the inward pointing links and therefore, the density ρ at that node is defined. By doing so zero normal momentum is achieved. Subsequently, the net tangential momentum at the surface is redistributed to the unknown links which have a tangential component. For velocity boundaries, populations are either added or redistributed to the unknown links to yield the prescribed velocity.

Maier et al.[26] have noted that certain wall geometries (e.g. convex edge and convex corner) cannot satisfy the no-slip condition under this scheme because there are insufficient unknown populations to define such a condition, resulting in curved instead of sharp-edged boundary. For sharp-orifice type problems (which are the primary focus of the present study), the shear layer formed downstream of the jet plane is sensitive to the sharpness at the orifice edges. To recover sharp orifice effect accurately, a new treatment is proposed for these boundary nodes. No-slip is achieved by averaging and redistributing the populations of known opposite link pairs. This new treatment (for the known links) in conjunction with the bounce-back scheme (which solves for the unknown links) eliminates all net momentum contribution of all opposite links pairs while preserving the total population at the boundary node. Specific examples on how this scheme is applied to no-slip walls of different orientation are presented in the Appendix A.

3 Numerical Implementation

There are some specific issues that need to be addressed before LBE-LES can be implemented to study the flows of interest. These implementation issues are discussed here.

3.1 Lattice Stretching

Since f_α are continuous distribution functions, lattice stretching is possible in LBE-LES. He et al.[27] proposed a new Interpolation Supplemented Lattice-Boltzmann Equation (ISLBE) for nonuniform mesh grids. Analysis of the new algorithm scheme has shown that as long as second-order interpolation is employed and the flow domain is appropriately discretized, the overall scheme maintains good (second-order) accuracy while exhibiting improved numerical stability.[28,29] Stretching has the obvious advantage of allowing a finer lattice in regions of high shear and coarser grid in region of lesser importance. In this study, the ISLBE method is implemented using the Lagrangian upwind quadratic interpolation method.

It was also determined in the earlier study[29] that very large stretching of the lattice results in an effective increase in the numerical dissipation which may degrade accuracy. Therefore, the stretching factor and the associated loss in accuracy need to be balanced. Results here suggest that stretching below 10% is reasonable and can be used without compromising accuracy.

3.2 Inflow Turbulence

To simulate high Reynolds number jet, realistic inflow condition must be prescribed at the inlet. Obviously, the inflow domain is a truncation of the entire length of the pipe which represents the source of the jet because it is impossible to simulate the entire inflow domain with available computational resources. Note that, in all the simulations here, the actual conditions

at the jet exit plane is not modeled since it is part of the simulation domain.

To simulate a fully developed turbulent inflow, turbulence is synthesized by a method similar to that of Lee et al.[30] The resulting velocity field is nearly Gaussian, conforms to a specified energy spectrum, has a pre-specified turbulence intensity, is divergence free and is non-periodic in time.

For the square jet explicit coherent forcing is also implemented. This is described below.

3.3 The Square Jet and Jet in Crossflow

The forced square jet investigated here is similar to the configuration studied earlier numerically and experimentally.[14, 31] The inflow jet profile is:

$$\mathbf{u}(t,x,y) = w_{\text{inflow}}(x,y) + Aw_{\text{inflow}}(x,y)sin(\omega_t t) + \mathbf{V_p}(\mathbf{t},\mathbf{x},\mathbf{y}) \quad (12)$$

where w_{inflow} is the prescribed inflow velocity profile, Aw_{inflow} the forcing amplitude and $\mathbf{V_p}$ the synthesized turbulence. The w_{inflow} profile is parabolic with a boundary layer thickness of $0.85D_e$ with respect the flat sides of the pipe where D_e is the equivalent diameter of the square pipe. The other flow parameters such as the Reynolds number, Strouhal number and streamwise velocity fluctuation intensity, etc. are all also chosen to match experimental data.[14]

The jet in crossflow test conditions were also chosen to match a recent set of experiments.[16] More details are given below.

3.4 Grid Resolution and Numerical Stability

For LES, a key issue is that the numerical dissipation of the scheme needs to be smaller than the subgrid dissipation. In addition, the subgrid model needs to provide adequate dissipation when the resolution is insufficient to resolve all scales. Thus, the choice of the subgrid model then becomes critical. With the dynamic Smagorinsky's model employed here, relatively high resolution is still needed since this model implicitly assumes that production and dissipation of kinetic energy is in equilibrium at the unresolved (i.e., subgrid scales). However, this assumption is only valid when the grid resolution is fine enough to allow the cutoff to occur in dissipation scales. This requirement implies that very high grid resolution will be needed when high Re flows have to be simulated. It is expected, that the use of the k_{sgs} based LDM model[9, 23] has the ability to capture higher Re flows with coarser grid since the equilibrium assumption is not needed and hence, the cutoff can be in the inertial range.

Another general observation is that for a given Re the lattice resolution has to be larger than the equivalent finite-volume resolution if the stretching has to be minimized (note that in the non-dimensional form the minimum lattice size is unity). However, the LBE-LES is computationally much more efficient and therefore, this increase in resolution is not a major hinderance.

3.5 Parallel Implementation and Performance

To expedite the turn around time, the LBE-LES solver is implemented in parallel on distributed memory parallel processing computers using the Message Passing Interface (MPI). The computational domain is decomposed into smaller sub domains. Optimization requires proper programming of all the boundary conditions and minimizing message passing overhead.

The parallel LBE-DNS version of the solver exhibits good scalability as shown in Fig. 2. This data is obtained on the Cray T3E and the result seems to suggest a super-linear scalability of the solver which seems to increase as the number of processors exceed 100. Note that the baseline configuration is 3 processors. The super linear behavior is attributed to the better use of cache memory when the computational domain is divided into smaller equal chunks. Obviously, this performance will be different on alternate MPI machines with different cache structure.

The computational efficiency of the solver is considerable. For the forced square jet a maximum resolution of 11 million grid points have been used for the simulations. On IBB SP4 the LBE-LES solver (with the localized dynamic option) costs around 4.42×10^9 CPU seconds per time step per grid point per processor. For a typical simulation of 20 forcing cycles, approximately 2500 single-processor hours are needed.

4 Results and Discussion

Here, we discuss the square jet and JICF in separate sections.

4.1 The Square Jet

The dimensions of the square jet computational domain are shown in Fig. 3 and are similar to the geometry of the laboratory experimental jet facility employed earlier[14] except for the fact that the pipe cross section is circular in the experiments, whereas it is a square in the present simulation. The equivalent diameter of the pipe is matched to yield equivalent cross sectional area. A range of grid resolutions have been used for these simulations. The base grid resolved the inlet pipe, the nozzle and the outflow domains using $108 \times 108 \times 48$, $50 \times 50 \times 6$ and $180 \times 180 \times 108$, respectively. The grid stretched from the high resolution in the orifice region but the stretching is maintained below 10% to ensure accuracy is not compromised. A much higher resolution of $170 \times 170 \times 52$, $66 \times 66 \times 7$ and $202 \times 202 \times 234$ were also employed for the three regions in some of the simulations. Most of large-scale features are invariant in both resolution. However, with the finer grid the stretching could be reduced, the sharp orifice edge is better resolved, and more finer scale features are resolved.

Figure 4 compares ν_τ/ν and Ω/Ω_{max} at the same instance in time at the cross section of the orifice flat sides. Dissipation regions are maximum in the high

strain regions that typically reside in the braid regions and in the regions surrounding the vortices. The spatial variation of the subgrid eddy viscosity in space is also determined in part by the dynamic evaluation of the model coefficient.

The visualization of the evolution of the CS is shown in Fig. 5. The primary vortex structures and the hairpin vortices are evident in the near field of the exit plane. However, these CS break down rapidly into fine scale structures due to shear layer instability generated by turbulence. Closer examination shows that the jet undergoes two axis switching in the initial region of jet growth. Beyond the second location rapid breakdown of the structures into smaller, 3D randomly oriented vortices.

Figure 6 shows the time-averaged jet half-width spreading rate in the side and diagonal planes. The previous simulation using MILES-NS is also shown. Axis switching is indicated by the cross-over of the spreading rate of the jet in the two planes. In the near field region of the jet exit, the profiles of LBE-LES exhibit more rapid crossovers whereas those of MILES-NS remain relatively flat within the region $z/D_e < 1.0$. Comparison with experiments show that the LBE-LES prediction of axis switching compares favorably. The vortex structure at the corners are formed further downstream with respect to the sides. This triggers the axis switching more quickly (than a nominally flat velocity profile) since it results in the formation of non-planar vortex structure. For the structure formed from a uniform analytic profile (as in the earlier numerical study), axis switching only occurs after the vorticity field is sufficiently coherent to invoke non-uniform induction of the flowfield. This result indicates the importance of capturing the flow dynamics at the jet exit plane (note that in MILES-NS, inflow is prescribed at this location). Since the present study allows for boundary layer growth in the inlet pipe, the conditions at the exit plane evolve naturally and more realistically. This lead to a more natural growth and breakdown of the shear layer structures.

There are some discrepancies as well. The LBE-LES jet-half width magnitude is lower than in the previous data. This may suggest a slower spreading of the jet in the current simulation. The growth rate in the far field is also slower than the experiment. This may be due to lattice stretching and a lack of resolution in the far field. We will revisit this issue at a later stage.

4.2 Jet in Cross-flow

In this study, the experiment of Ajersch *et al.*[16] is chosen as the benchmark case for validation. The dimensions of the computational domain are shown in Fig. 7. The simulation is carried out at Reynolds number of 4700 based on the jet velocity and the nozzle width D and at jet-cross-flow velocity ratio of 0.5. The cross-flow velocity profile is initialized with a boundary layer thickness of $2D$. The computational domain is resolved using $200 \times 150 \times 100$ for the cross-flow domain and $50 \times 50 \times 100$ for jet section. So a total of 3.25×10^6 grid points is used to discretize the domain. Computations for a full simulation (which includes five flow through times) requires approximately 400 single-processor hours with 2.3×10^9 memory on the Compaq SC45 machines. Periodic boundaries are used in the cross-stream boundaries of the cross-flow domain to simulate a single square jet out of a row of six used in the experiment. On the top surface free slip and for exit surface, outflow conditions has been considered. The incoming pipe velocity profile with constant value is prescribed in the pipe a distance of 10D below the flat plate allowing the flow to develop naturally as the jet merges into the cross-flow.

Results are compared with the experiment of Ajersch and numerical results obtained by Hoda *et al.*[17] Standard $k-\epsilon$ model of Lam and Bremhorst,[32] high-Re, $k-\epsilon$ model of Launder-Tselepidakis[33] and two-layer turbulence model of Chen[34] have been used in Hoda *et al* studies. For sake of brevity, we identify experiments, Lam-Bremhorst, Launder-Tselepidakis and Lattice Boltzmann Equation methods, by EXPR, LB, LT and LBE, respectively, in the following figures.

4.2.1 Flow features in JICF

Jet in crossflow generates a complex flow topology due to the highly 3D nature of this flow. Past studies have identified two structural features called horse-shoe (or kidney-shaped) structure and counter rotating vortex pair (CRVP) (see Fig. 8) that form in this flow. As shown, the current simulation has captured the entire dynamics of the formation of these structures and their subsequent breakdown. Figure 8 shows these features quite clearly. This figure also shows how jet roles up and create the recirculation region, which is the important mechanism for mixing of jet and cross-flow.

Figure 9 shows the iso-surface of vorticity structures in vertical, span-wise and stream-wise direction (only the positive iso-surface of stream-wise vorticty is shown). The green iso-surface marks regions in the flow where $|w_x| = 0.01$, the blue surface marks the same magnitude for $|w_y|$ and the red surface marks the same magnitude for $|w_z|$. These structure have been called, hanging vortices (w_x), span-wise rollers (w_y) and vertical streaks (w_z).[35]

For example, the hanging vortices are tube-like structures that form directly above the exit on the lateral edges of the jet and extending around the jet body and then up along the lee-side of the jet approximately matching the path of the jet. These tubes coincide with the location where the jet shear layer fold thereby emanating vortices, which eventually contribute to the circulation of the counter-rotating vortex pair (CVP).

Figure 10 shows two sets of instantaneous stream-

lines. One set originates within the jet, and the second set originates from the crossflow boundary layer upstream of the jet exit. These lines also collect in the hanging vortex. The vorticity carried by the hanging vortex provides the circulation necessary to create the CVP. The CVP changes position and strength with time and streamwise location.

4.2.2 Comparison with experiments

The mean stream-wise velocity profile comparisons are presented at various stream-wise stations ($x/D = 0, 1, 3, 5$) along the jet center plane ($y/D = 0$) in Fig. 11. The exit plane velocity is well captured by LBE-LES and the reverse flow at $x/D = 1$ is also captured, albeit smaller in size. Further downstream the boundary reattach and continues to grow. In general, all methods (past and current) show reasonable agreement.

Figure 12 shows the mean stream-wise velocity profiles at different stream-wise locations but along the edge of the jet ($y/D = -0.5$). Since there is no direct interaction between jet and cross-flow at the edges, cross-flow deflection is less compared to the deflection at the center plane. Reverse flow is not seen at this plane and this agrees with experimental data.

The mean wall-normal velocity profiles along the jet center plane and along the jet edge are shown in Figs. 13 and Fig. 14, respectively. The agreement is good in the jet exit and close to the orifice. However, it deteriorates further downstream even though the over trends are captured reasonably well.

Other mean flow properties show similar qualitative and quantitative agreement with experimental data. The scatter between the various methods is not significant to determine which method is superior. However, it can be noted that the LBE-LES model gives a reliable prediction of this flow at all locations, thereby establishing its viability.

Turbulent kinetic energy (TKE) profiles at the jet center plane are shown in Fig. 15. According to Hoda *et al*,[17] TKE is produced not only during interaction between the crossflow boundary layer and the jet but also due to various velocity gradients and strong streamline curvature. Peak of TKE profile is located at the same location of maximum velocity gradients. TKE is larger at the top of the jet where the interactions are dominant (see discussion on coherent structures above). Comparison (not shown) of turbulence fluctuation intensity in the stream-wise (u_{rms}/W_j) and wall-normal (w_{rms}/W_j) directions shows that these fluctuation levels are similar in magnitude but that there are significant anisotropy in the near-wall region. This is to be expected since in this region vortical breakdown occurs in a complex 3D manner.

Finally, Fig. 16 shows the normalized shear stress ($u_{rms}w_{rms}/W_j$) profiles along the centerline. Although the general trend is similar to the experiment, the LES-LBE predictions are significantly larger in many regions. In general, the Reynolds stress prediction in highly separated flow regions is very difficult and the Smagorinsky's model used here is not very reliable in such regions (with and without the localized dynamic evaluation). It is expected that improved predictions will be possible for all properties once the LBE-LES approach is extended to use the subgrid kinetic energy closure.[23] This effort is underway and will be reported soon.

5 Conclusions

A new LES implementation of the Lattice Boltzmann Equation method is developed and used to simulate 3D square jet and a 3D square jet in cross-flow. A localized dynamic subgrid closure using the algebraic eddy viscosity model is used to close the LES version of the LBE model. The configurations and test conditions are chosen to compare with data wherever possible. In these simulations the inflow is applied far upstream of the jet exit plane and this allows the jet exit profile to evolve naturally.

Simulation of the square jet shows that the shed coherent structures undergo multiple axis switching in the jet increasing the effective mixing. The locations and the overall growth rate are in good agreement with measurement. JICF results were also compared with data and with other numerical method results. Good agreement with data is again obtained in the present study. These results establish LBE-LES as an alternate method for simulating turbulent shear flows. The strengths and limitations of the LBE-LES are also discussed.

6 Acknowledgement

This work is supported in part by Army Research Office and NASA Glenn Research Center. Computational time was provided by Department of Defense High Performance Computing Centers at ERDC (MS) and NAVO (MS).

References

[1] Zinn, B. and Neumeier, Y., "Control of combustion instabilities with secondary fuel injection using real time modes observation: practical implementation," *Proceedings of the Combustion Institute*, Vol. 26, 1996.

[2] Pashereit, C. O., Gutmark, E., and Weisenstein, W. W., "Structure and control of thermoacoustic instablities in a gas-turbine combustor," *Combustion Science and Technology*, Vol. 138, 1998, pp. 213–232.

[3] Paschereit, C., Gutmark, E., and Weisenstein, W. W., "Coherent structures in swirling flows and their role in acoustic combustion control," *Physics of Fluids*, Vol. 11, 1999, pp. 2667–2678.

[4] Wang, H. and Menon, S., "Fuel-air mixing enhancement by synthetic microjets," *AIAA Journal*, Vol. 39, No. 12, 2001, pp. 2308–2318.

[5] McNamara, G. and Zanetti, G., "Use of the Boltzmann equation to simulate lattice-gas automata," *Physical Review Letters*, Vol. 61, 1988, pp. 2332–2335.

[6] Higuera, F., Jimenez, J., and Succi, S., "Boltzmann approach to lattice gas simulations," *Europhysics Letters*, Vol. 9, 1989, pp. 663–668.

[7] Chen, H., Chen, S., and Matthaeus, W., "Recovery of the Navier-Stokes equations using a lattice-gas Boltzmann method," *Physical Review A*, Vol. 45, 1992, pp. 5339–5342.

[8] Chen, S. and Doolen, D., "Lattice Boltzmann method for fluid flows," *Annual Review of Fluid Mechanics*, Vol. 30, 1998, pp. 329–364.

[9] Kim, W.-W., Menon, S., and Mongia, H., "Numerical simulations of reacting flows in a gas turbine combustor," *Combustion Science and Technology*, Vol. 143, 1999, pp. 25–62.

[10] Grinstein, F., "Self-induced vortex ring dynamics in subsonic rectangular jet," *Physics of Fluids*, Vol. 7, No. 10, 1995, pp. 2519–2521.

[11] Gutmark, E. and Schadow, K., "Flow characteristics of orifice and tapered jets," *Physics of Fluids*, Vol. 30, No. 11, 1987, pp. 3448–3454.

[12] Ho, C. and Gutmark, E., "Vortex induction and mass entrainment in a small-aspect-ratio elliptic jet," *Journal of Fluid Mechanics*, Vol. 179, 1987, pp. 383–405.

[13] Grinstein, F. F., "Vortex dynamics and entrainment in rectangular free jets," *Journal of Fluid Mechanics*, Vol. 437, 2001, pp. 69–101.

[14] Grinstein, F. F., Gutmark, E., and Parr, T., "Near field dynamics of subsonic free square jets. A computational and experimental study," *Physics of Fluids*, Vol. 7, No. 6, 1995, pp. 1483–1497.

[15] Miller, R., Madnia, C., and Givi, P., "Numerical simulation of non-circular jets," *Computers and Fluids*, Vol. 24, No. 1, 1995, pp. 1–25.

[16] Ajresch, P., Zho, J., Ketler, S., Salcudean, M., and Gartshore, I., "Multiple jets in a crossflow: detailed measurments and numerical simulations," *Journal of Turbomachinery*, Vol. 119, 1997, pp. 330–342.

[17] Hoda, A., Acharya, S., and Tyagi, M., "Reynolds strees transport model predictions and large eddy simulations for film coolant jet in crossflow," *Proceedings of ASME TURBOEXPO 2000*, 2000, pp. 1–15.

[18] Qian, Y., d'Humierès, D., and Lallemand, P., "Lattice BGK models for the Navier-Stokes equation," *Europhysics Letters*, Vol. 17, 1992, pp. 479–484.

[19] Bhatnagar, P., Gross, E., and Krook, M., "A model for collision process in gases. I. Small amplitude process in charged and neutral one-component system," *Physical Review A*, Vol. 94, 1954, pp. 551–525.

[20] Frisch, U., Hasslacher, B., and Pomeau, Y., "Lattice-gas automata for the Navier-Stokes equations," *Physical Review Letters*, Vol. 56, 1986, pp. 1505–1508.

[21] Qian, Y., S., S., and Orszag, S., "Recent advances in lattice Boltzmann computing, In Stauffer, D., editor," *Annual reviews of computational physics III*, 1995, pp. 195–242.

[22] Mei, R., Shyy, W., Yu, D., and Luo, L., "Lattice Boltzmann method for 3D flows with curved boundary," *Journal of Computational Physics*, Vol. 161, 2000, pp. 680–699.

[23] Kim, W.-W. and Menon, S., "A new incompressible solver for large-eddy simulations," *International Journal of Numerical Methods in Fluids*, Vol. 31, 1999, pp. 983–1017.

[24] Zou, Q. and He, X., "On pressure and velocity boundary conditions for the lattice Boltzmann BGK model," *Physics of Fluids*, Vol. 9, No. 6, 1997, pp. 1591–1598.

[25] Noble, D. R., Chen, S., Georgiadis, J. G., and Buckius, R. O., "A consistent hydrodynamic boundary condition for the lattice Boltzmann mehtod," *Physics of Fluids*, Vol. 7, No. 1, 1995, pp. 203–209.

[26] Maier, R. S., Bernard, R. S., and Grunau, D. W., "Boundary conditions for the lattice Boltzmann method," *Physics of Fluids*, Vol. 8, No. 7, 1996, pp. 1788–1801.

[27] He, X., Luo, L., and Dembo, M., "Some progress in lattice Boltzmann method: Part I. Nonuniform grids," *Journal of Computational Physics*, Vol. 129, No. 2, 1996, pp. 357–363.

[28] He, X., "Error analysis for the interpolation supplemented lattice Boltzmann equation scheme," *International Journal of Modern Physics C*, Vol. 8, No. 4, 1997, pp. 737–745.

[29] He, X., Luo, L., and Dembo, M., "Some progress in lattice Boltzmann method: Enhancement of Reynolds number in simulations," *Physica A*, Vol. 239, 1997, pp. 276–285.

[30] Lee, S., Lele, S., and Moin, P., "Simulation of spatially evolving turbulence and the applicability of Taylor's hypothesis in compressible flows," *Physics of Fluids A*, Vol. 4, 1992, pp. 1521–1530.

[31] Grinstein, F. and DeVore, C., "Dynamics of coherent structures and transition to turbulence in free square jets," *Physics of Fluids*, Vol. 8, No. 5, 1996, pp. 1237–1251.

[32] Lam, C. K. G. and Bremhorst, K. A., "Modified form of the k- Model for predicting wall turbulence," *Journal of Fluid Engineering*, Vol. 103, 1981, pp. 456–460.

[33] Launder, B. E. and Tselepidakis, D. P., "Contribution to the second-moment modeling of sublayer turbulent transport," *Near-Wall Turbulence, Hemisphere*, 1990, pp. 818–833.

[34] Chen, H. C., "Submarine Flows Studied by second Moment closure," *Journal of Engineering Mechanics*, Vol. 121, 1995, pp. 1136–1146.

[35] Yuan, L., Street, R., and Ferziger, J., "Large-eddy simulations of a round jet in crossflow," *Journal of Fluid Mechanics*, Vol. 379, 1999, pp. 71–104.

Appendix: Boundary Conditions

Here, specific examples on the implementation of the various boundary conditions used are given. The convention of the link vectors used in the examples is illustrated in Figure 1 and their surface orientations in Figure 17.

For the planar node, if a normal velocity w_{bc} is prescribed, the tangential momentums of the parallel links and the density are:
$u_{tan} = (f_1 + f_7 + f_9) - (f_2 + f_8 + f_{10})$
$v_{tan} = (f_3 + f_7 + f_1 0) - (f_4 + f_8 + f_9)$
$\rho = (2(f_6 + f_{12} + f_{13} + f_{16} + f_{17} + f_0 + f_1 + f_2 + f_3 + f_4 + f_7 + f_8 + f_9 + f_{10})/(1 - w_{bc})$.

The unknown populations are:
$f_5 = f_6 + \rho w_{bc}$
$f_{11} = f_{12} - 0.5u_{tan}$
$f_{14} = f_{13} + 0.5u_{tan}$
$f_{15} = f_{16} - 0.5v_{tan}$
$f_{18} = f_{17} + 0.5v_{tan}$.

For nodes on concave edge, the tangential momentum is: $v_{tan} = f_3 - f_4$ and the unknowns:
$f_1 = f_2$, $f_5 = f_6$, $f_{11} = f_{12}$
$f_7 = f_8 - 0.25v_{tan}$
$f_9 = f_{10} + 0.25v_{tan}$
$f_{15} = f_{16} - 0.25v_{tan}$
$f_{18} = f_{17} + 0.25v_{tan}$.

The *buried* links (links that do not participate in streaming but in collision) are averaged and redistributed: $f_{13} = f_{14} = 0.5(f_{13} + f_{14})$.

For the concave corner, all the class I links exist in known/unknown pairs, and thus:
$f_1 = f_2$, $f_3 = f_4$, $f_5 = f_6$, $f_7 = f_8$
$f_{11} = f_{12}$, $f_{15} = f_{16}$
$f_9 = f_{10} = 0.5(f_9 + f_{10})$
$f_{13} = f_{14} = 0.5(f_{13} + f_{14})$
$f_{17} = f_{18} = 0.5(f_{17} + f_{18})$.

Earlier studies[26] pointed out that convex edges and convex corners cannot satisfy the no-slip condition with this scheme because there are insufficient unknown populations (at least one class I link) at these boundaries. New treatments are devised for these boundaries, and the no-slip condition is enforced by modifying the known populations, as well as the unknowns. In short, the unknown populations are computed using bounce-back and the known non-parallel populations of opposite links averaged and redistributed. Subsequently, the momentum of the parallel links is redistributed to the non-parallel pairs. With this method, the total population of the known links is preserved. For the geometry in Figure 17 $f_{11} = f_{12}$ and $v_{tan} = f_3 - f_4$. The others are:
$f_1 = f_2 = 0.5(f_1 + f_2)$
$f_5 = f_6 = 0.5(f_5 + f_6)$
$f_{13} = f_{14} = 0.5(f_{13} + f_{14})$
$f_7 = 0.5(f_7 + f_8) - 0.125v_{tan}$
$f_8 = 0.5(f_7 + f_8) + 0.125v_{tan}$
$f_9 = 0.5(f_9 + f_{10}) + 0.125v_{tan}$
$f_{10} = 0.5(f_9 + f_{10}) - 0.125v_{tan}$
$f_{15} = 0.5(f_{15} + f_{16}) - 0.125v_{tan}$
$f_{16} = 0.5(f_{15} + f_{16}) + 0.125v_{tan}$
$f_{17} = 0.5(f_{17} + f_{18}) - 0.125v_{tan}$
$f_{18} = 0.5(f_{17} + f_{18}) + 0.125v_{tan}$.

For the convex corner, there are no unknowns and therefore, all the opposite link pairs are averaged and redistributed.

For the symmetric boundary condition, the unknown populations beyond the plane of symmetry are needed during streaming. Thus, the outgoing populations are reflected back into the domain exactly the opposite way they leave. For the geometry in Figure 17, using k to denote the known outgoing populations at the i plane and uk to denote the incoming unknowns at $i + 1$:
$f_2^{uk,i+1} = f_1^{k,i}$
$f_8^{uk,i+1} = f_9^{k,i}$
$f_{10}^{uk,i+1} = f_7^{k,i}$
$f_{12}^{uk,i+1} = f_{13}^{k,i}$
$f_{14}^{uk,i+1} = f_{11}^{k,i}$.

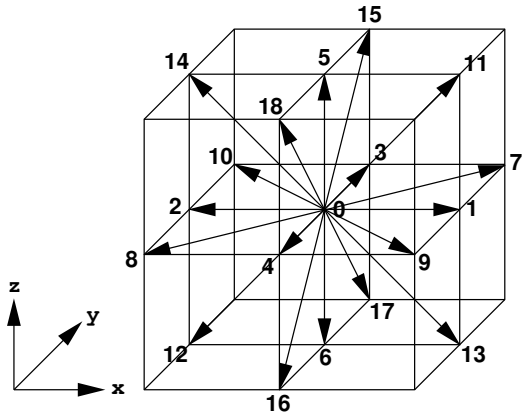

Fig. 1 Link vectors of f_α.

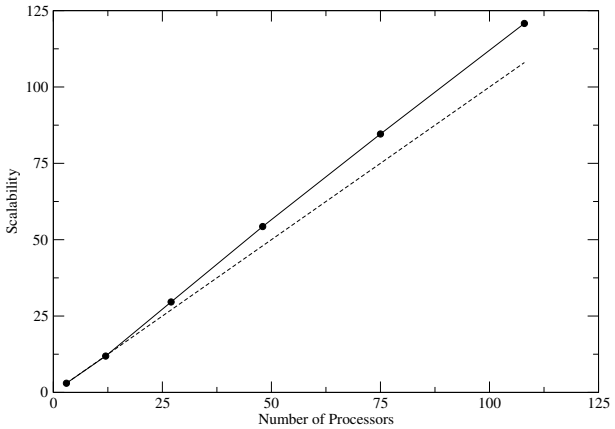

Fig. 2 Parallel scalability of the LBE solver. The super-linear behavior is due to better use of cache memory as the local lattice size decreases.

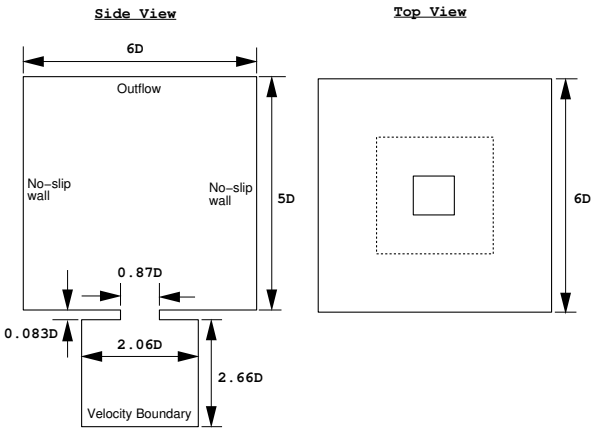

Fig. 3 Computational domain for the square jet.

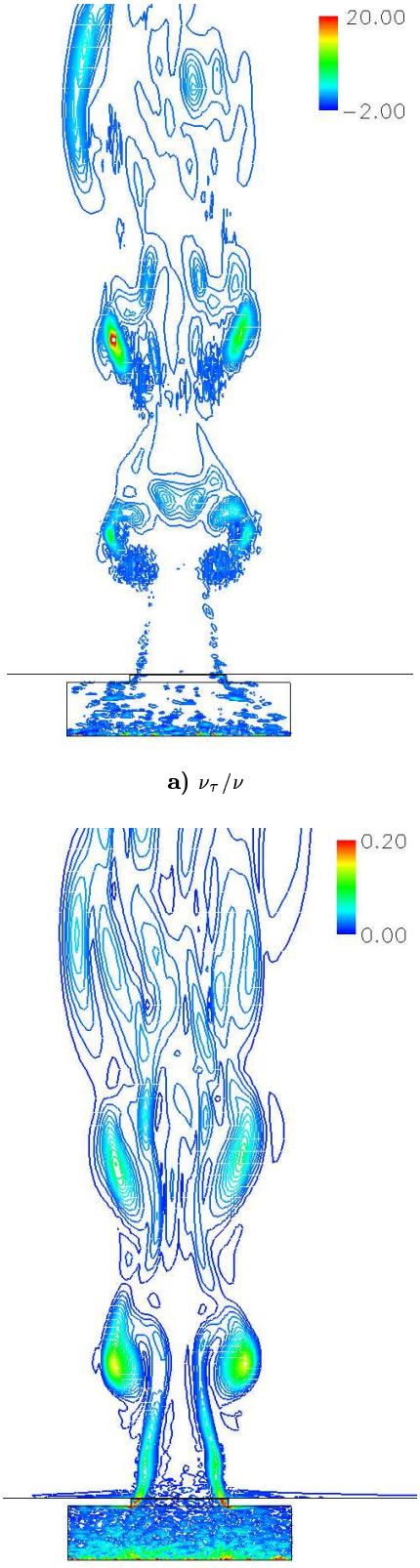

a) ν_τ/ν

b) Ω/Ω_{max}

Fig. 4 Instantanous ν_τ/ν and Ω/Ω_{max} at the same instant.

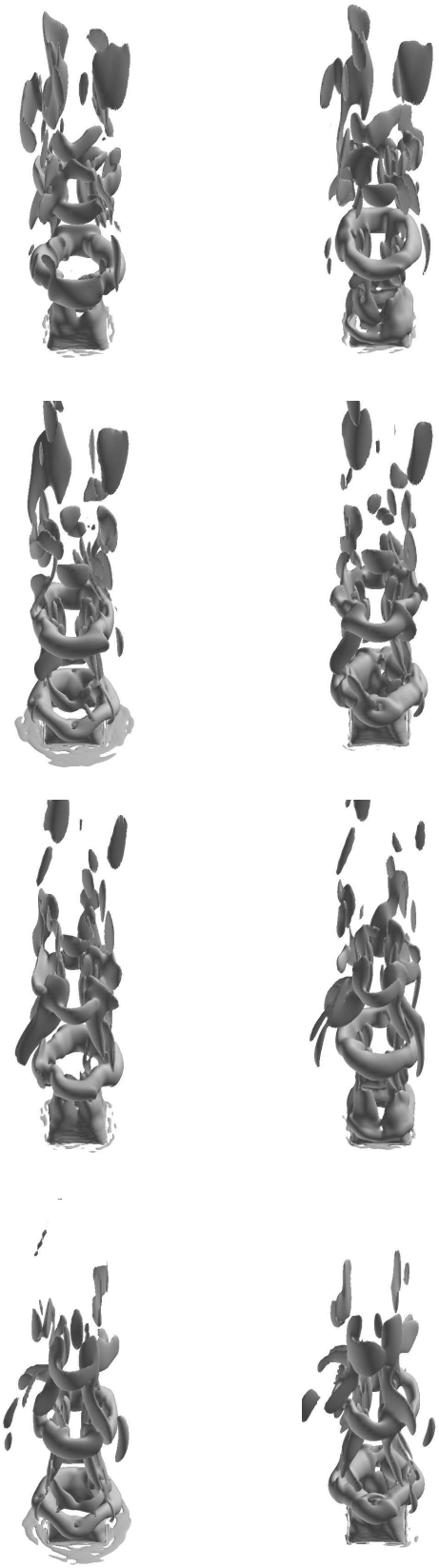

Fig. 5 Square jet flow evolution over two forcing cycle. Isosurface of the vorticity magnitude at temporal intervals of $\omega t = \pi/2$ are shown.

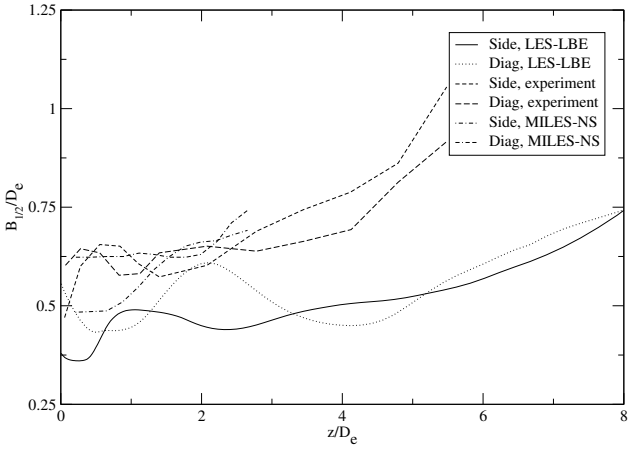

Fig. 6 Axial evolution of the jet half-width. The current LBE-LES and the earlier numerical result are compared with experimental data.

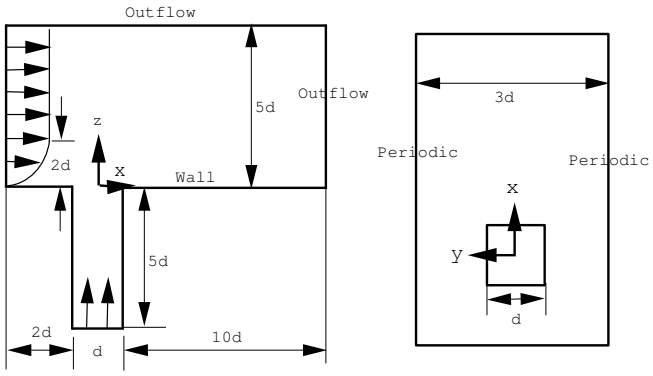

Fig. 7 Geometry and computational domain for the jet in crossflow.

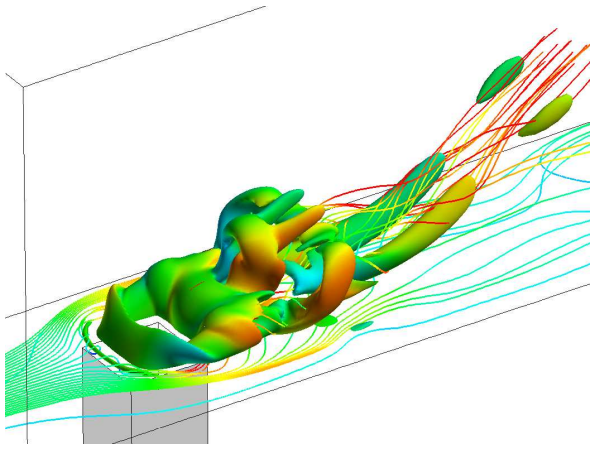

Fig. 8 Instantaneous vorticity magnitude isosurface $|w| = 0.003$ super-imposed by vertical vorticity as a scalar. Contours of span-wise vorticity are in gray color. Horse-shoe structure (near the wall) and CRVP (following the jet trajectory) are observed.

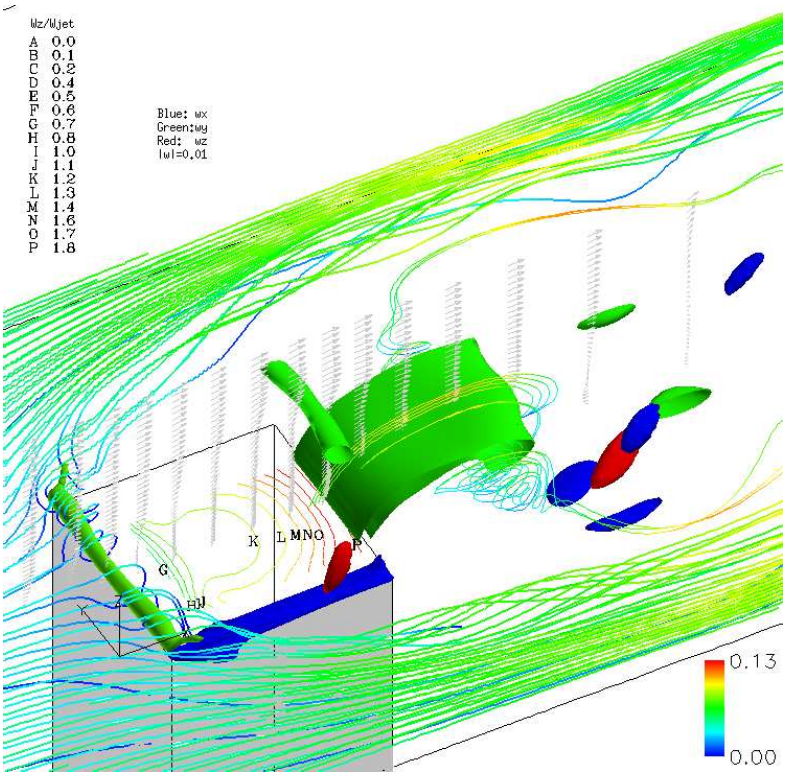

Fig. 9 Isosurfaces of vorticity. Green: $|w_x| = 0.01$, blue: $|w_y| = 0.01$, red: $|w_z| = 0.01$.

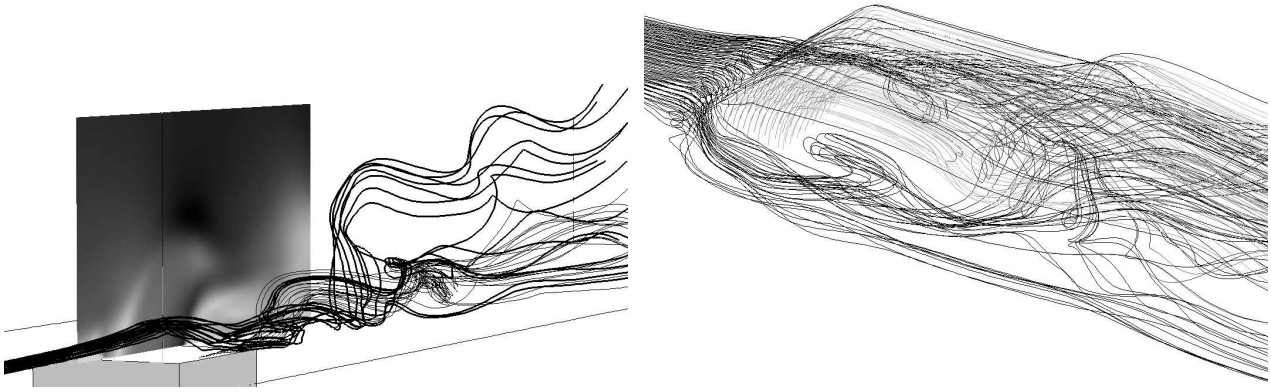

a) Flow through hanging vortex **b)** Flow in the wake of the jet

Fig. 10 Instantaneous streamlines pattern in the side and wake of the JICF.

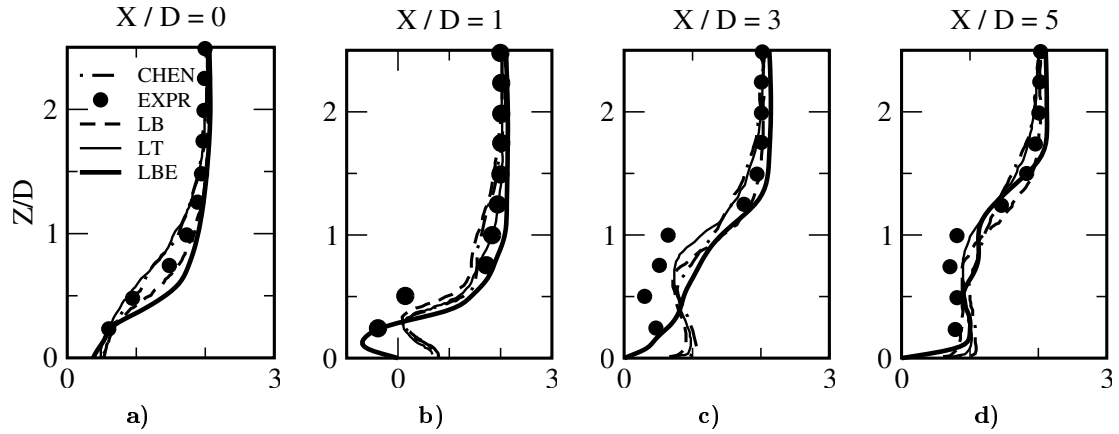

Fig. 11 Mean stream-wise velocity profiles (U/W_j)along the jet center plane (y/D=0) at x/D=0,1,3,5 from the jet center.

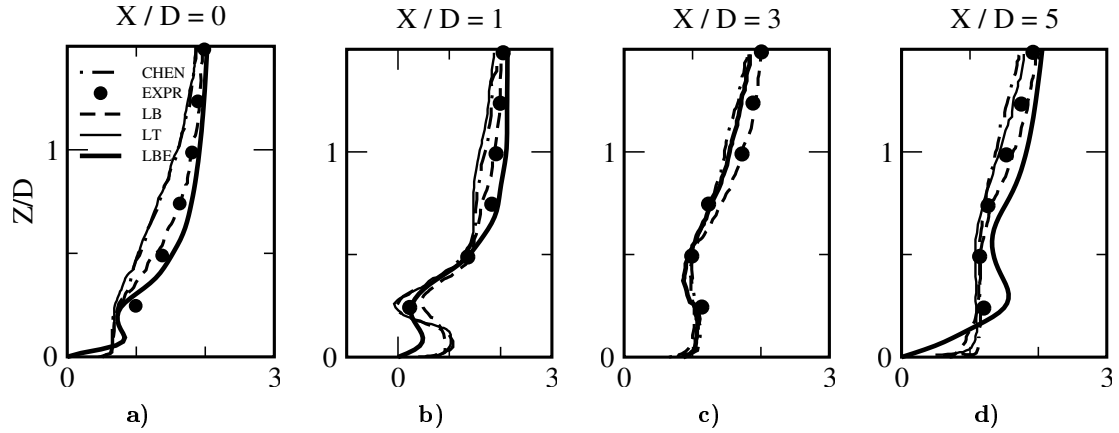

Fig. 12 Mean stream-wise velocity profiles (U/W_j)along the jet edge plane (y/D=-0.5) at x/D=0,1,3,5 from the jet center.

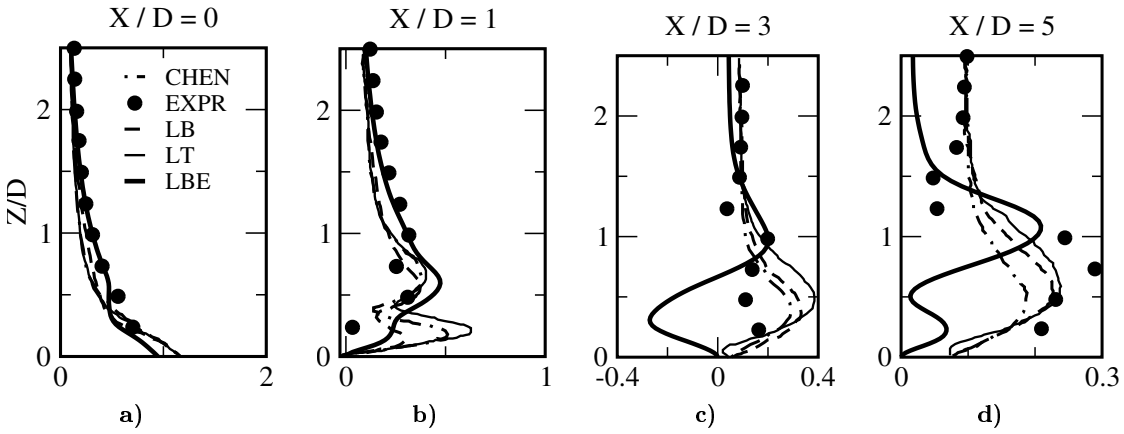

Fig. 13 Mean wall-normal velocity profiles (W/W_j)along the jet center plane (y/D=0) at x/D=0,1,3,5 from the jet center.

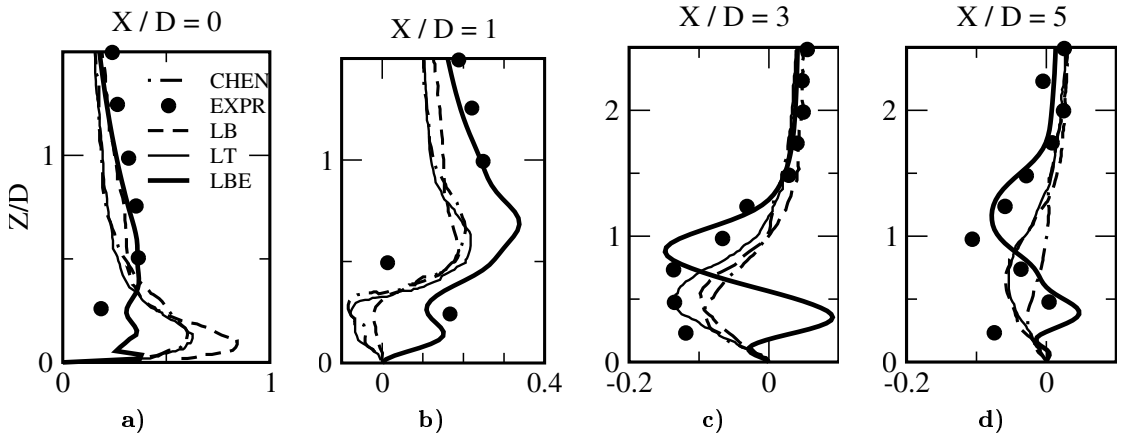

Fig. 14 Mean wall-normal velocity profiles (W/W_j)along the jet edge plane (y/D=-0.5) at x/D=0,1,3,5 from the jet center.

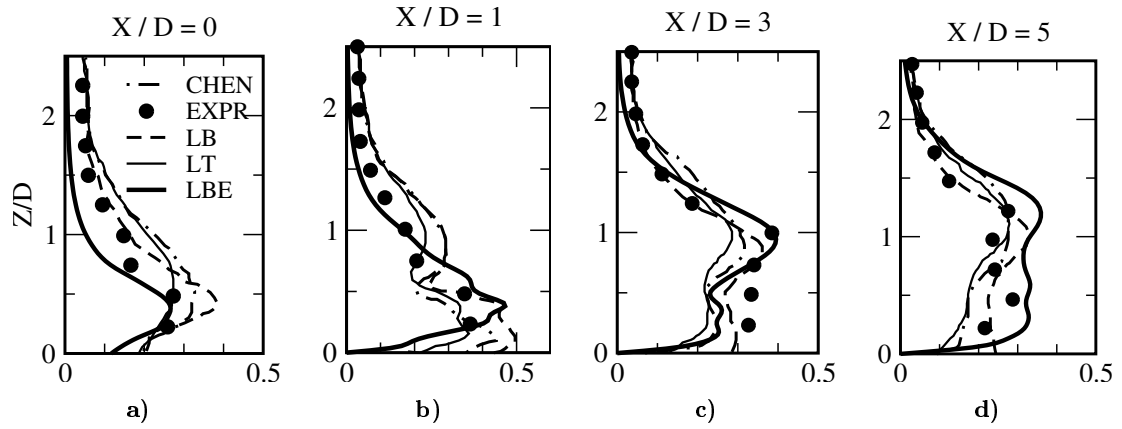

Fig. 15 Mean turbulence kinetic energy $\sqrt{k}/W_j$ along the jet center plane (y/D=0) at x/D=0,1,3,5 from the jet center.

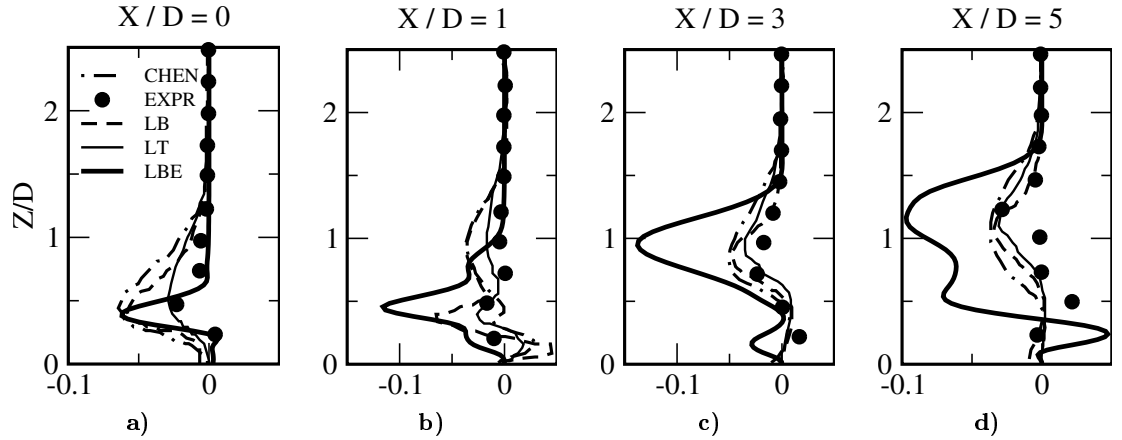

Fig. 16 Turbulence shear stress uw/W_j^2 profiles along the jet edge plane (y/D=0) at x/D=0,1,3,5 from the jet center.

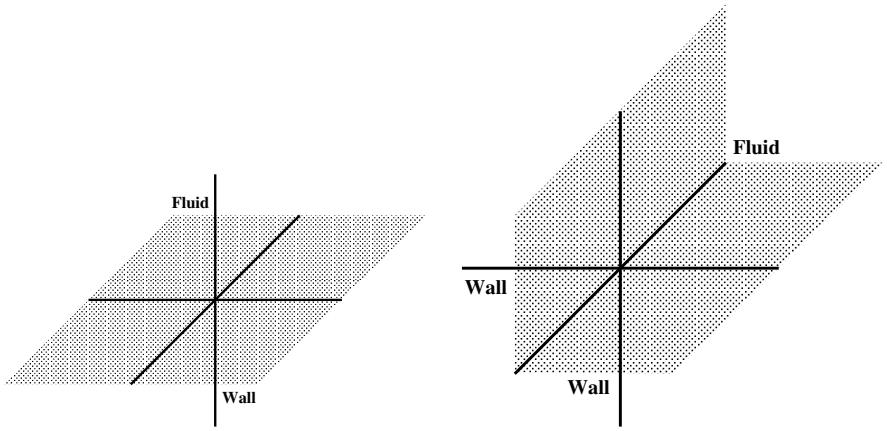

a) Planar surface

b) Concave edge

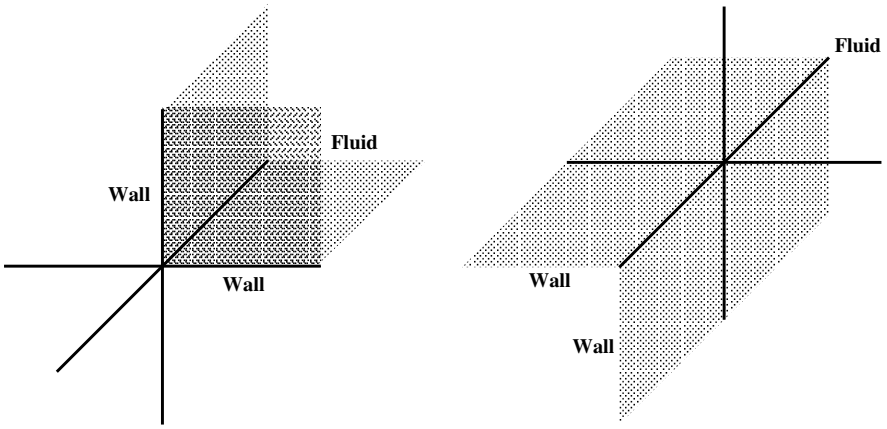

c) Concave corner

d) Convex edge

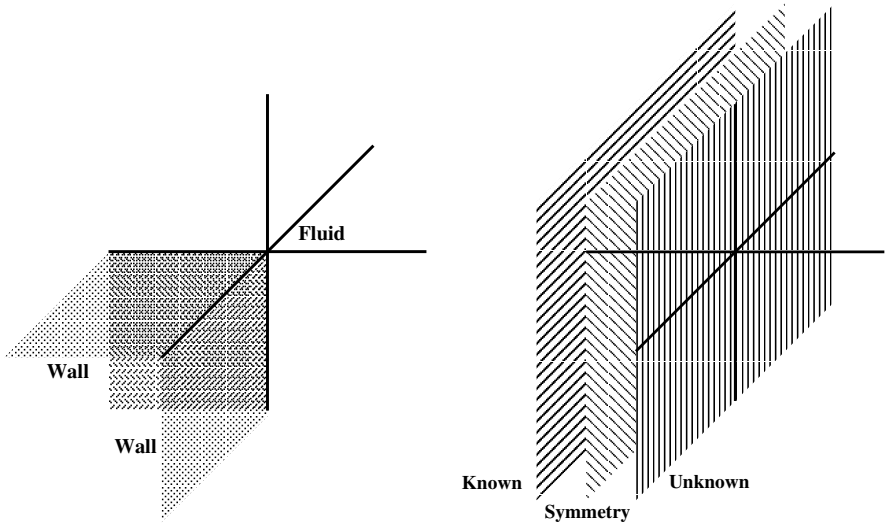

e) Convex corner

f) Symmetric plane

Fig. 17 Boundary geometries.